

Electronic Supplementary Information (ESI)

Interfacial engineered RDX/TATB energetic co-particles for enhanced safety performance and thermal stability

Yanzhou Qu ^{a,b}, Wei Qian ^b, Jianhu Zhang ^b, Feiyan Gong ^b, Zhengfeng Xie ^a, Zhijian Yang ^b,

Fude Nie ^{b*}, Xu Zhao ^{b*}

^a Oil & Gas Field Applied Chemistry Key Laboratory of Sichuan Province, College of Chemistry and Chemical Engineering, Southwest Petroleum University, Chengdu 610500, China.

^b Institute of Chemical Materials, China Academy of Engineering Physics, Mianyang 621900, China. Email: xuzhao@caep.cn, niefude@caep.cn

Characterizations

The morphologies and microstructures of all the samples were studied by scanning electron microscopy (SEM, Sigma HD, ZEISS) under an acceleration voltage of 3kV. High-performance liquid chromatography (HPLC, Agilent LC1260 series, Agilent Technologies, USA) were conducted to evaluate the real content of the RDX/TATB co-particles. Each content was calculated through their average value. X-ray computed tomography (X-ray CT), a three-dimensional (3D) and non-destructive imaging technology have been adopted to verify the surface and the internal microstructure. LSM900 MAT laser scanning confocal microscope (CLSM) was adopted to obtain the high-resolution surface 3D morphology of the RT-24 co-particle. Specific surface areas and pores distribution were analyzed using a multipoint Brunauer-Emmett-Teller (BET) method. X-ray diffraction (XRD) was performed

adopting a PANalytical X'Pert Pro diffractometer with Cu K α radiation ($\lambda = 0.154056$ nm). All the diffraction peaks have been calibrated using standard crystalline silicon. Fourier-transform infrared (FT-IR) spectrum were interpreted on a Nicolet Fourier Spectrophotometer-360 using KBr pellets. The surface elements of samples were tested by an ESCALAB 250 Xi X-ray photoelectron spectrometer (XPS, Thermal fisher, scientific UK) with the Al K α radiation of 1486.6 eV. Thermal decomposition behavior of the obtained samples was analyzed by utilizing a simultaneous thermal gravimetric analysis (TGA) and differential scanning calorimeter (DSC) performed on METTLER TG-DSC. The measurements used 40 mL min⁻¹ high-purity N₂ ambient purge for 50-500 °C with a sample mass of about 2.2 mg. The heating rates were set in 5, 10, 15, and 20 °C min⁻¹, respectively. The impact and friction sensitivity of samples were conducted by Bundesanstalt-für-Materialforschung (BAM, BFH-10, Czech) method to evaluate the mechanical safety performance of samples.

Simulation section

Molecular dynamics (MD) simulations were carried out to reveal the interfacial interactions between different RDX and TATB interfaces. The single crystal structure of α -RDX comes from experimental measurement and belongs to monoclinic system P_{21/C} space group. The unit cell parameters are a = 1.3182 nm, b = 1.1574 nm and c = 1.0709 nm, $\alpha = \beta = \gamma = 90^\circ$ (*Acta Cryst.* **1972**, 28(9): 2857). TATB single crystal belongs to the P₁ space group of triclinic system. The unit cell parameters are a = 0.9010 nm, b = 0.9028 nm and c = 0.6812 nm, $\alpha = 108.58^\circ$, $\beta = 91.82^\circ$, $\gamma = 119.97^\circ$ (*Acta Cryst.* **1965**, 18, 485-496). The dominant

growth planes and crystal habits of RDX and TATB were predicted by Bravais-Friedel Donnay-Harker (BFDH) method (*Bull. Soc. Fr. Mineral.*, **1907**, 30, 326).

The unit cell of RDX was further expanded to a 3*3*3 supercell, and it was cleaved along main crystalline directions (2 1 0), (1 1 1), (0 0 2), (0 2 1) and (1 0 2) separately to form crystal surface model, while TATB was further expanded to 3*3*5 model and cleaved along (1 0 0), (0 1 0) and (0 0 1). Each RDX surface model was put on to each TATB surface to form a crystalline interface model, and 15 interface models were constructed.

The molecular mechanics (mm) structure optimization and energy minimization are carried out under compass force field (*Comput. Theor. Polym. Sci.* **1998**, 8, 229). The molecular dynamics simulation (MD) of canonical ensemble is carried out for the optimized model. The temperature is set to 298 K (25 °C), and the nose method is used to control the temperature (*J. Chem. Phys.* **1984**, 81, 511-519). A total of 200ps MD simulation was carried out to ensure the equilibrium for both temperature and energy. The simulation results were analyzed to obtain the interaction situations between RDX and TATB. The interaction energies between RDX and TATB surfaces were obtained according to the energies of equilibrium models (E_{inter}) as follows:

$$E_{\text{inter}} = [E_{\text{total}} - (E_{\text{RDX}} + E_{\text{TATB}})]/S$$

where E_{inter} , E_{total} , E_{RDX} and E_{TATB} are the interaction energy, total system and subsystem energy, respectively.

The energy of the optimization model and the change of interaction energy and the contribution of van der Waals force (VDW) and electrostatic force (ES) to the interaction have been calculated and studied.

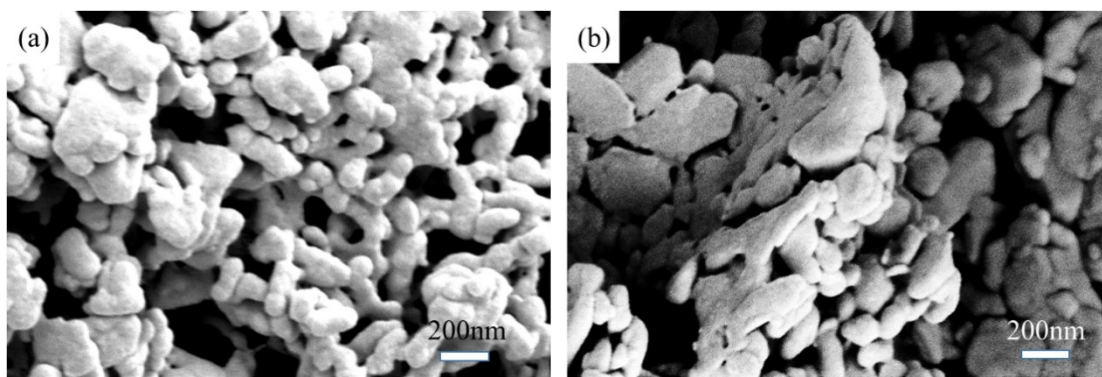


Fig. S1. SEM images of neat TATB (a) before and (b) after hydrothermal treatment.

Explanation: Dense intramolecular/intermolecular hydrogen bonds of TATB crystal make TATB hard to be stimulated under thermal and pressure. Therefore, TATB crystal is only slightly grown, not as obvious as RDX. Such similar results have also been observed in our previous work [*Chemical Engineering Journal* **2020**, 387, 124209].

Table S1. The abbreviation of samples along various hydrothermal treatment time.

| hydrothermal time | 1h | 3h | 6h | 12h | 18h | 24h |
|-------------------------|------|------|------|-------|-------|-------|
| abbreviation of samples | RT-1 | RT-3 | RT-6 | RT-12 | RT-18 | RT-24 |

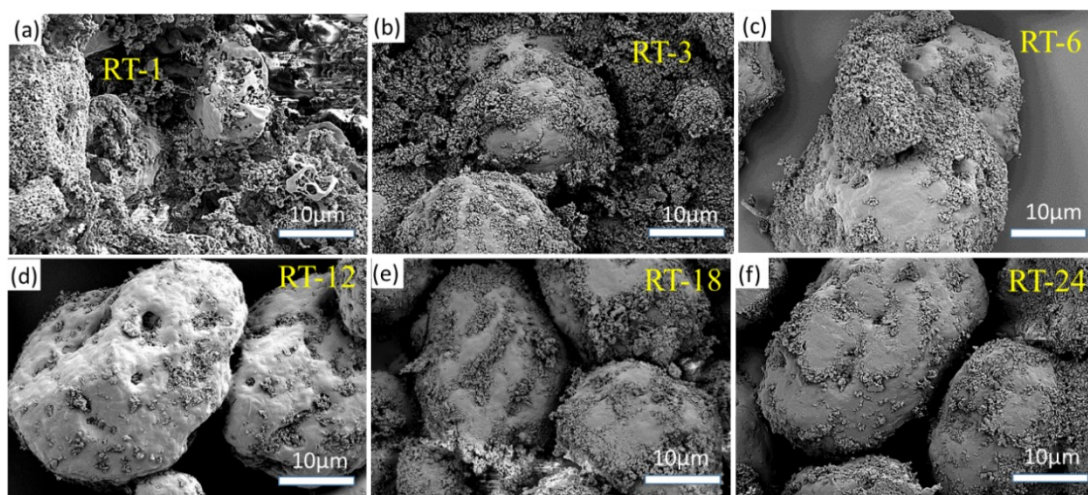


Fig. S2. The SEM images of as-prepared RDX/TATB co-particles at different hydrothermal treatment time with 1 h to 24 h.

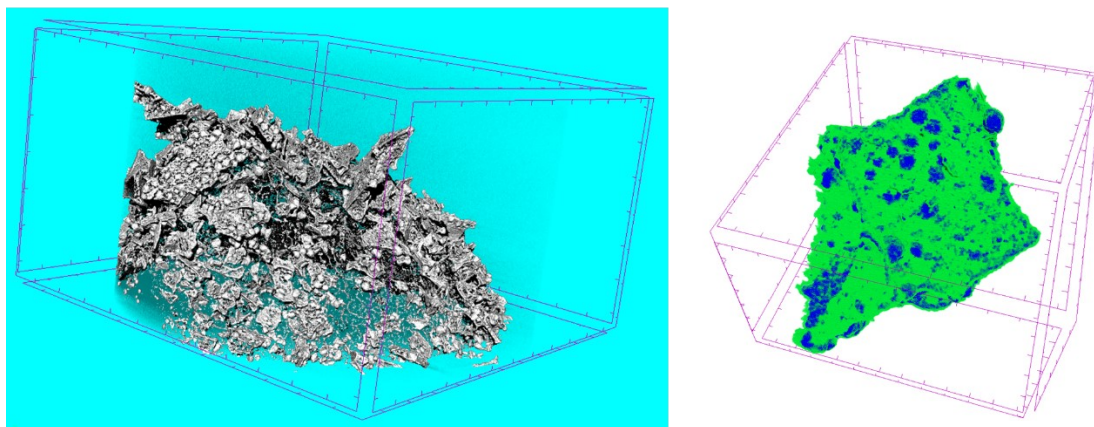


Fig. S3. The overall CT modelled image and the inside CT modelled image of RT-mix, where the blue and green part represents to TATB and RDX, respectively.

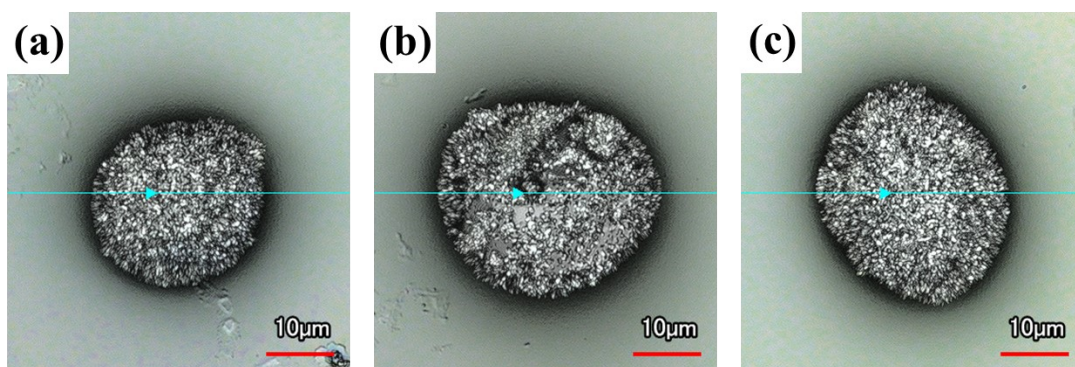


Fig. S4. a, b and c show the laser images of the RT-24 co-particle. The horizontal line is the profile of the cross section of the co-particles.

Table S2. The specific surface area and pore volume of RT-24 co-particle and samples

| Samples | Specific surface area (m ² g ⁻¹) ¹⁾ | Pore volume (cm ³ g ⁻¹) |
|---------|--|--|
| RDX | 1.9325 | 0.003535 |
| RT-mix | 3.3881 | 0.010256 |
| RT-24 | 1.1430 | 0.004582 |

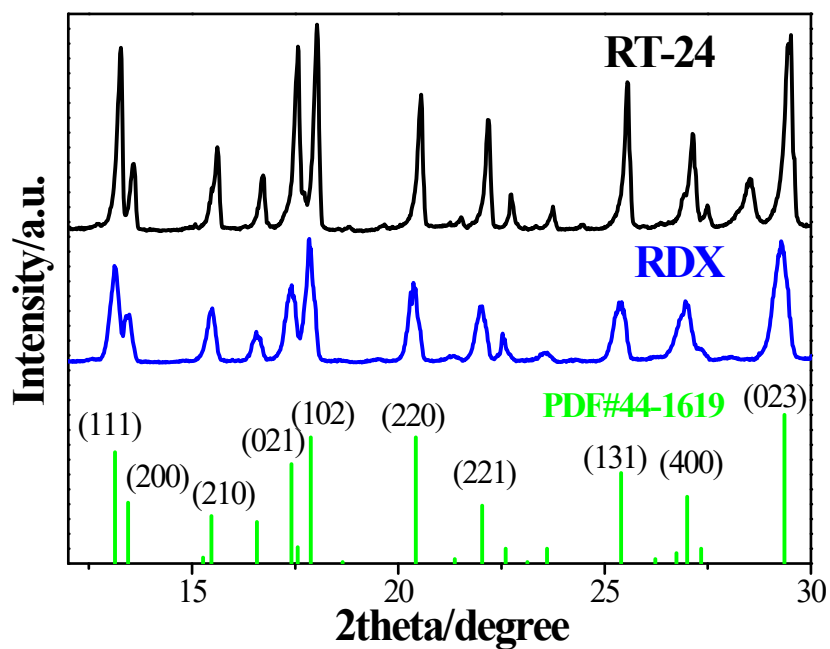


Fig. S5. The XRD patterns of as-prepared RT-24 co-particle and RDX compare with standard PDF card of RDX.

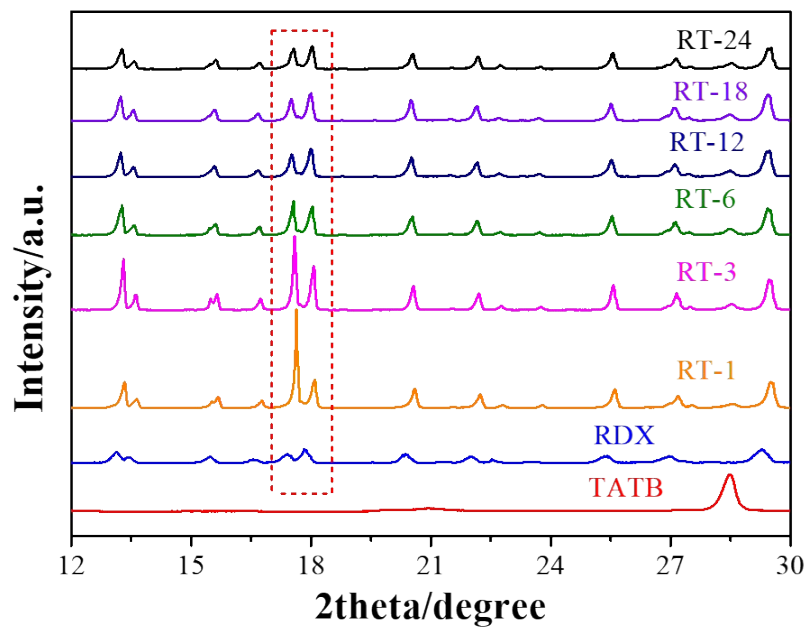


Fig. S6. The XRD patterns of as-prepared RDX/TATB co-particles at different hydrothermal treatment time from 1h to 24h, as well as raw materials RDX, TATB.

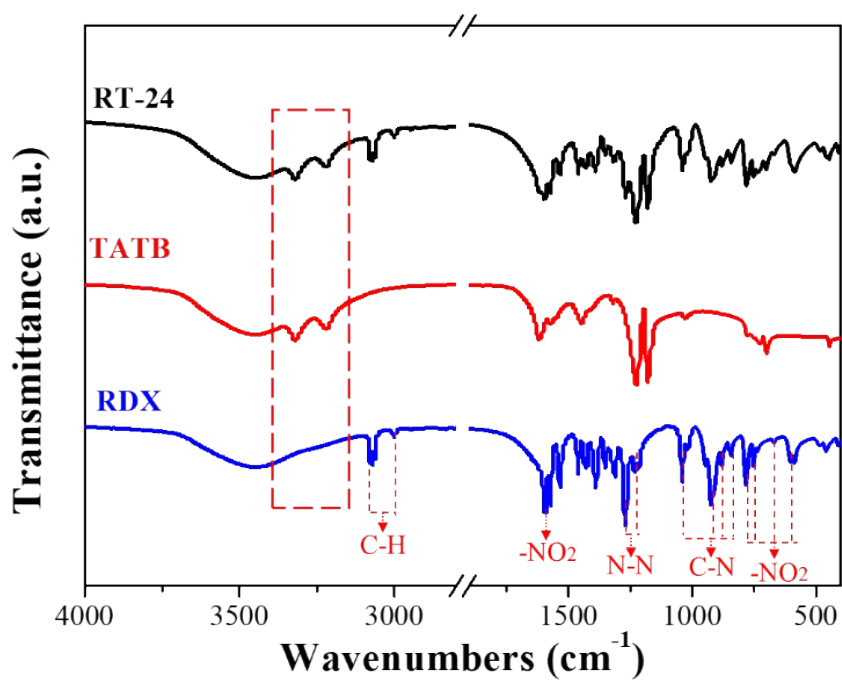


Fig. S7. The FTIR spectra of raw RDX, TATB, as well as RT-24 co-particle.

Table S3. Interfacial interaction energies at the RDX-TATB interfaces.

| Energy [kcal/mol per nm ²] | E_{inter} | E_{vdw} | E_{ES} | E_{other} |
|--|--------------------|------------------|-----------------|--------------------|
| RDX (2 1 0)-TATB (0 0 1) | -55.278 | -25.792 | -26.840 | -2.646 |
| RDX (1 1 1)-TATB (0 0 1) | -52.296 | -23.119 | -25.453 | -3.723 |
| RDX (0 0 2)-TATB (0 0 1) | -49.230 | -22.227 | -23.038 | -3.966 |
| RDX (0 2 1)-TATB (0 0 1) | -56.720 | -26.037 | -27.112 | -3.571 |
| RDX (1 0 2)-TATB (0 0 1) | -57.380 | -27.404 | -28.462 | -1.514 |
| RDX (2 1 0)-TATB (0 1 0) | -55.888 | -26.013 | -27.887 | -1.988 |
| RDX (1 1 1)-TATB (0 1 0) | -59.584 | -27.162 | -29.155 | -3.268 |
| RDX (0 0 2)-TATB (0 1 0) | -59.262 | -34.935 | -21.652 | -2.675 |
| RDX (0 2 1)-TATB (0 1 0) | -60.806 | -34.930 | -23.249 | -2.627 |
| RDX (1 0 2)-TATB (0 1 0) | -61.291 | -32.200 | -24.898 | -4.193 |
| RDX (2 1 0)-TATB (1 0 0) | -59.694 | -26.155 | -30.997 | -2.541 |
| RDX (1 1 1)-TATB (1 0 0) | -60.781 | -29.134 | -28.136 | -3.511 |
| RDX (0 0 2)-TATB (1 0 0) | -64.905 | -36.055 | -25.966 | -2.884 |
| RDX (0 2 1)-TATB (1 0 0) | -64.983 | -36.974 | -25.869 | -2.141 |
| RDX (1 0 2)-TATB (1 0 0) | -65.395 | -36.791 | -27.038 | -1.566 |

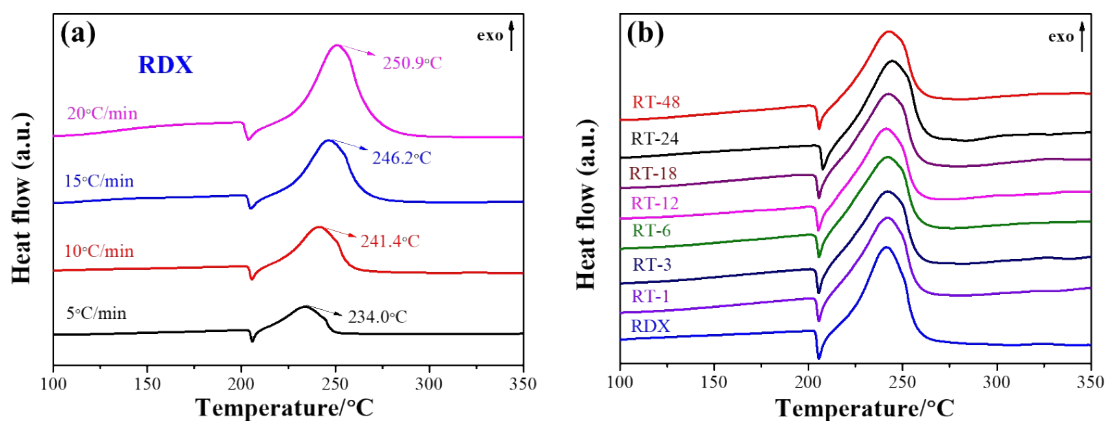


Fig. S8. Non-isothermal DSC curves of (a) RDX under different heating rates from 5 to 20 °C min⁻¹ and (b) resultant RT-x of different hydrothermal treatment time under heating rate of 10 °C min⁻¹.

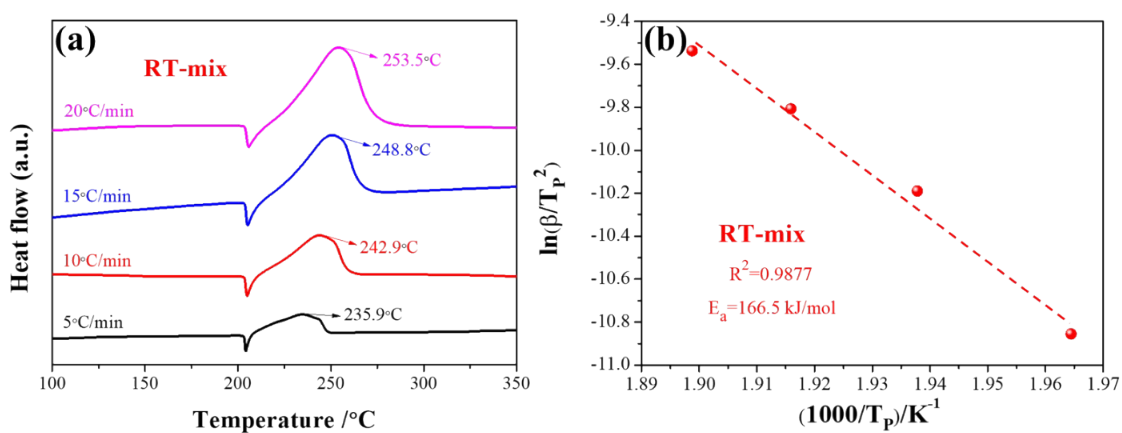


Fig. S9. (a) Non-isothermal DSC curves of RT-mix under different heating rates from 5 to 20 °C min⁻¹ and (b) Fitting curve of RT-mix based on Kissinger method.

Table S4. Comparison of the improved exothermic decomposition temperature of RT-24 co-particle and other reported composite explosives.

| Samples | T_p (°C) | ΔT (°C) | Additives (wt%) | References |
|------------------------|---------------------------|----------------|------------------------|--|
| RT-24 | 244.4 | 3.0 | 10 | This work |
| RDX@CNF | 241.5 | 1.0 | 3.33 | <i>Langmuir</i> . 2021 , 37, 8486. |
| RDX/GAP | 242.3 | 1.1 | 40 | <i>J. Energ. Mater.</i> 2019 , 37, 80. |
| RDX/F2604 | 244.5 | 1.5 | 10 | <i>J. Energ. Mater.</i> 2018 , 36, 223. |
| RDX/BAMO-THF | 243.2 | 2.0 | 20 | <i>J. Energ. Mater.</i> 2018 , 36, 424. |
| RDX/DOS | 245.16 | 2.16 | 10 | <i>Defence Technol.</i> 2017 , 13, 263. |
| qy-HMX | 285.1 | 1.7 | 6.1 | <i>Chem. Eng. J.</i> 2020 , 390, 124565. |
| CL-20/TNT | 254.71 | 1.02 | 25 | <i>Defence Technol.</i> 2021 , 17, 1936. |
| CL-20/BAMO-THF | 244.3 | 2.5 | 45 | <i>Defence Technol.</i> 2019 , 15, 306. |
| Cellulose/CL-20 | 244.22 | -0.12 | 5 | <i>Cryst. Growth Des.</i> 2020 , 20, 6811. |
| CL-20/PNCB | 242.5 | -1.7 | 24.3 | <i>Materials.</i> 2018 , 11, 1130. |
| Cellulose/HMX | 280.92 | -1.85 | 5 | <i>Mater. Chem. Phys.</i> 2021 , 257, 123700. |

Table S5. Thermal analysis parameters of as prepared RT-x co-particles at different hydrothermal treatment time from 1 to 24 hours compare to pristine RDX as well as RT-mix.

| Samples | Exothermic | | | | |
|---------|------------------|-----------|-----------|----------------|------------|
| | β /°C /min | T_i /°C | T_p /°C | ΔT /°C | ΔH |
| RDX | 10 | 205.7 | 241.4 | 0 | 1389 |
| RT-1 | 10 | 205.6 | 242.0 | +0.6 | 1313 |
| RT-3 | 10 | 205.6 | 242.2 | +0.8 | 1187 |
| RT-6 | 10 | 205.5 | 241.7 | +0.3 | 1353 |
| RT-12 | 10 | 205.2 | 241.2 | -0.2 | 1261 |
| RT-18 | 10 | 205.6 | 242.2 | +0.8 | 1329 |
| RT-24 | 10 | 205.2 | 244.4 | +3 | 1680 |
| RT-mix | 10 | 205.0 | 242.9 | +1.5 | 1386 |

Notes: β , the heating rates, T_i , the onset temperature, in °C, T_p , the exothermic peak temperature, in °C, ΔH , heat releases, in $J g^{-1}$, ΔT , temperature differences between the exothermic peaks with and without TATB, in °C.

Table S6. Thermal decomposition temperature by DSC, calculated Kissinger E_a of RT-mix,

RDX and RT-24 co-particle.

| Samples | β /°C/min | T_P /°C | T_P /K | $1000/T$ /K ⁻¹ | $\ln(\beta/T^2)$ | E_a /kJ/mol | R^2 |
|-----------------|-----------------|-----------|----------|---------------------------|------------------|---------------|--------|
| RT-mix | 5 | 235.9 | 509.05 | 1.964444 | -10.8557 | 166.5 | 0.9877 |
| | 10 | 242.9 | 516.05 | 1.937797 | -10.1898 | | |
| | 15 | 248.8 | 521.95 | 1.915892 | -9.80709 | | |
| | 20 | 253.5 | 526.65 | 1.898794 | -9.53734 | | |
| Pure RDX | 5 | 234.0 | 507.15 | 1.971803 | -10.8482 | 174.8 | 0.9904 |
| | 10 | 241.4 | 514.55 | 1.943446 | -10.1840 | | |
| | 15 | 246.2 | 519.35 | 1.925484 | -9.79711 | | |
| | 20 | 250.9 | 524.05 | 1.908215 | -9.52744 | | |
| RT-24 | 5 | 235.0 | 508.15 | 1.967923 | -10.8521 | 160.5 | 0.9665 |
| | 10 | 244.4 | 517.55 | 1.932180 | -10.1956 | | |
| | 15 | 250.9 | 524.05 | 1.908215 | -9.81512 | | |
| | 20 | 252.0 | 525.15 | 1.904218 | -9.53164 | | |

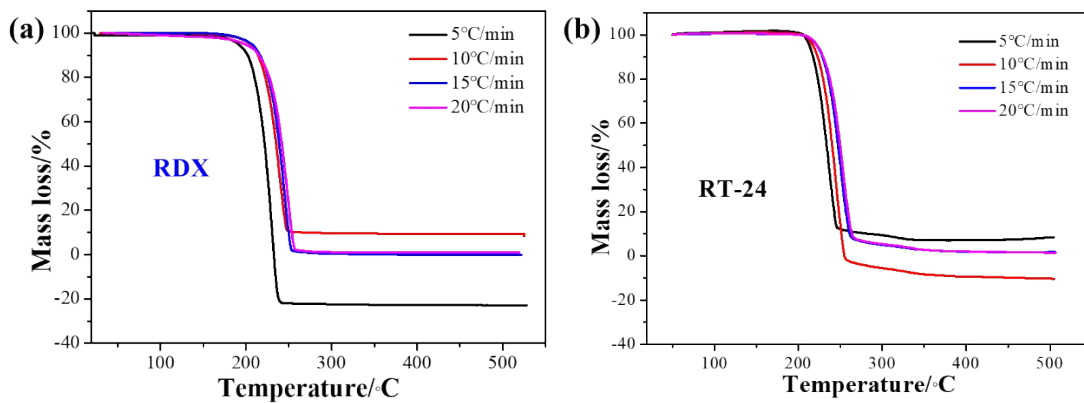


Fig. S10. The non-isothermal TG curves of (a) RDX and (b) RT-24

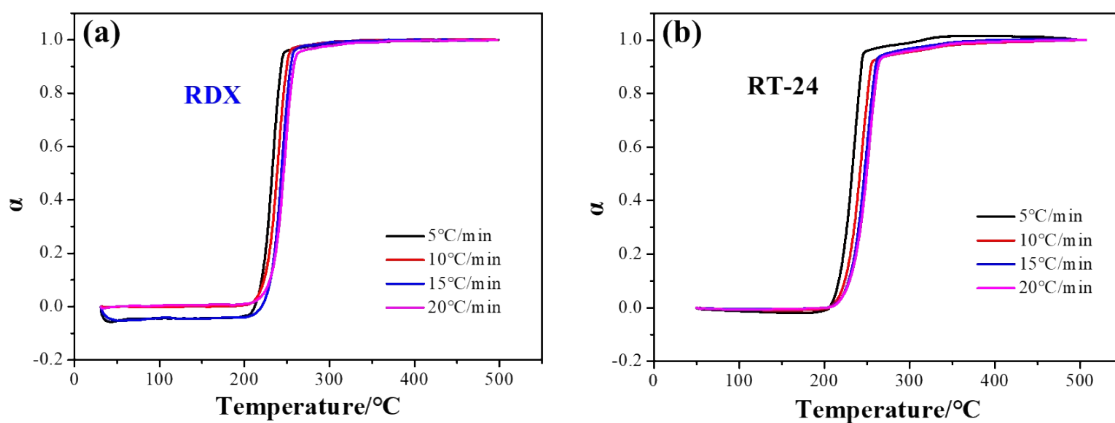


Fig. S11. The extent of conversion (α) versus temperature curves of (a) RDX and (b) RT-24

co-particle

Table S7. Date of RT-24 co-particle determined by TG in different heating rates and calculated apparent energies E_0 using iso-conversional OFW methods.

| α | T_5/K | T_{10}/K | T_{15}/K | T_{20}/K | $E_0/kJ\ mol^{-1}$ | R^2 |
|-------------|---------|------------|------------|------------|--------------------|---------|
| 0.1 | 490.06 | 497.06 | 501.57 | 502.65 | 203.12 | 0.97668 |
| 0.2 | 495.5 | 503.75 | 508.76 | 510.5 | 177.81 | 0.98524 |
| 0.3 | 499.5 | 508.18 | 513.33 | 515.89 | 168.81 | 0.99445 |
| 0.4 | 502.78 | 511.75 | 517.1 | 519.47 | 166.98 | 0.99166 |
| 0.5 | 505.62 | 514.92 | 520.06 | 522.71 | 166.09 | 0.99262 |
| 0.6 | 508.27 | 517.88 | 523.26 | 525.9 | 162.49 | 0.99178 |
| 0.7 | 510.92 | 520.83 | 526.16 | 528.7 | 162.36 | 0.98891 |
| 0.8 | 513.65 | 523.93 | 529.28 | 532.16 | 158.66 | 0.99087 |
| 0.9 | 516.52 | 527.76 | 533.31 | 536.22 | 150.49 | 0.98675 |
| Mean | | | | | 168.53 | |

Table S8. Date of RDX determined by TG in different heating rates and calculated apparent energies E_0 using iso-conversional OFW methods.

| α | T_5/K | T_{10}/K | T_{15}/K | T_{20}/K | $E_0/kJ\ mol^{-1}$ | R^2 |
|-------------|---------|------------|------------|------------|--------------------|---------|
| 0.1 | 493.29 | 496.37 | 503.83 | 502.65 | 211.51 | 0.7645 |
| 0.2 | 497.59 | 502.38 | 508.77 | 509.72 | 207.52 | 0.9447 |
| 0.3 | 500.88 | 505.9 | 512.02 | 514.47 | 197.53 | 0.96607 |
| 0.4 | 503.16 | 508.98 | 514.5 | 516.86 | 201.11 | 0.98567 |
| 0.5 | 505.41 | 511.49 | 516.12 | 519.24 | 206.93 | 0.9949 |
| 0.6 | 507.67 | 513.52 | 518.59 | 521.69 | 204.66 | 0.98949 |
| 0.7 | 510.12 | 516.05 | 521.01 | 524.04 | 207.99 | 0.99171 |
| 0.8 | 512.83 | 518.98 | 524.18 | 527.58 | 199.12 | 0.98977 |
| 0.9 | 516.22 | 522.91 | 527.26 | 531.05 | 204.33 | 0.99535 |
| Mean | | | | | 204.52 | |

Notes: α was the conversion rate. T with the subscript 5, 10, 15, 20 were the temperature obtained at the heating rates of 5, 10, 15, 20 °C min⁻¹, respectively. E with the subscript O was the calculated activation energy by OFW methods.

Table S9. Brief comparison of the mechanical sensitivity of RT-24 co-particle with other explosives.

| Materials | Impact sensitivity (J) | Friction sensitivity (N) | Reference |
|--------------------------|-------------------------------|---------------------------------|--|
| RT-24 co-particle | 17.5 | 216 | This work |
| CL-20/rGO | 2.4 | 128 | <i>Propellants, Explosives, Pyrotechnics</i> . 2020 , 45, 1293-1299 |
| CL-20/TATB | 8.15 | NA | <i>Cryst. Res and Technol.</i> 2018 , 53, 1800189. |
| CL-20/FOX-7 | 13.13 | NA | <i>Defence Technol.</i> 2020 , 16, 188-200. |
| HMX/FOX-7 | 14.9 | NA | |
| CL-20/4,5-MDNI | 11 | NA | <i>Cryst. Growth Des.</i> 2018 , 18, 6399-6403. |
| CL-20/2,4-MDNI | 9 | NA | |
| CL-20/1,4-DNI | 10 | NA | <i>Cryst. Growth Des.</i> 2019 , 19, 4476. |